ATLAS CONF Note

ATLAS-CONF-2023-016

3rd April 2023

Search for dark photons in rare Z boson decays with the ATLAS detector

The ATLAS Collaboration

A search for the dark photon produced in association with the dark Higgs boson via rare decays of the Standard Model Z boson is presented using 139 fb^{-1} of $\sqrt{s}$ = 13 TeV proton–proton collision data recorded by the ATLAS detector at the Large Hadron Collider. The dark Higgs boson decays into a pair of dark photons and at least two of the three dark photons further decay into pairs of electrons and muons, resulting in at least two same-flavour opposite-charge lepton pairs in the final state. The average invariant mass of the two lepton pairs is used to discriminate signal from the background. The data are found to be consistent with the background prediction and upper limits are set on the dark photon coupling to the dark Higgs boson times the kinetic mixing between the Standard Model photon and the dark photon, $\alpha_D\epsilon^2$, in the dark photon mass range of $[5, 40]$ GeV, excluding the Υ mass window $[8.8, 11.1]$ GeV. These limits cover significantly wider mass ranges than previous experiments.

ATLAS-CONF-2023-016
03 April 2023

Overwhelming astrophysical evidence [1–4] supports the existence of dark matter (DM), and understanding its nature is one of the most important goals in particle physics. Dark matter is generally expected to interact very weakly with Standard Model (SM) particles. This motivates the extension of the SM with hidden or dark sectors (DS). One of the simplest examples is an additional $U(1)_{\mathrm{D}}$ gauge symmetry associated with a gauge boson, the dark photon A', that mediates DS-SM interactions. In the dark Abelian Higgs scenario, the $U(1)_{\mathrm{D}}$ symmetry group could be spontaneously broken by a Higgs mechanism through which the dark photon acquires a mass, adding a dark Higgs boson h_{D} to such models [5, 6].

The minimal A' model has three unknown parameters: the mass of the dark photon, $m_{A'}$; the effective coupling of the dark photon to SM particles, ϵ, induced via kinematic mixing with the SM photon; and the hidden-sector gauge coupling, α_D, which is the coupling of the A' to DS particles [5]. Dark photons will decay to visible SM particles, lepton pairs or hadrons, or invisible particles of the DS. Constraints have been placed on visible A' decays, in the parameter space of $m_{A'}$ and ϵ, by previous beam-dump, fixed-target and collider experiments [5, 7–11]. The dark Abelian Higgs model introduces two additional unknown parameters: the mass of the dark Higgs boson, $m_{h_{\mathrm{D}}}$, and the mixing between h_{D} and the SM Higgs boson. The Higgs-strahlung channel, where a dark photon is produced in association with a dark Higgs boson, has also been explored at low-energy electron-positron colliders via $e^+e^- \to A'h_{\mathrm{D}}$ [12, 13]. The Higgs-strahlung channel is sensitive to α_D, which is also the coupling of the A' to the h_{D}. Hence experimental evidence for a signal in this process would provide complementary information to direct searches for A'.

This note presents searches for the dark photon in rare decays of the Z boson $Z \to A'h_{\mathrm{D}}$, with the mass hierarchy of $m_{A'} + m_{h_{\mathrm{D}}} < m_Z$ and using at least two same-flavour opposite-charge lepton pairs in the final state. For the model considered [6], no mixing between the SM and dark Higgs bosons is assumed, and the A' is the lightest particle in the DS and invisible DS decays are kinematically forbidden. When kinematically allowed the dark Higgs boson can decay into one or two on-shell A' via $h_{\mathrm{D}} \to A'A'^{(*)}$, as illustrated in Fig. 1, and the A' in turn decays into SM fermions. The parameter space $m_{h_{\mathrm{D}}} > m_{A'}$ is explored in this search, giving the process of $pp \to Z \to A'h_{\mathrm{D}} \to A'A'A'^{(*)}$. Final states with at least two on-shell A' decaying fully leptonically, $A' \to \ell^+\ell^-(\ell = e, \mu)$, are used to search for the A'. In this scenario, the kinematic mixing ϵ is small, and thus the dark photon has a narrow total decay width narrower than 10^{-3} GeV, but ϵ is large enough to ensure that the dark photon decays promptly [14].

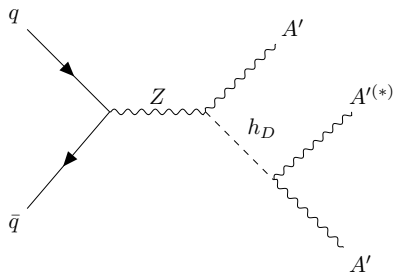

Figure 1: Feynman diagram illustrating the signal process $q\bar{q} \to Z \to A'h_{\mathrm{D}}$, $h_{\mathrm{D}} \to A'A'^{(*)}$.

The $\sqrt{s} = 13$ TeV proton-proton (pp) collision data used for this analysis were recorded by the ATLAS experiment at the Large Hadron Collider (LHC) during 2015-2018. The corresponding integrated luminosity is 139 fb^{-1} [15] after the application of data quality requirements [16]. A combination of single- and multi-lepton triggers [17, 18] is used. The ATLAS experiment at the LHC is a multipurpose particle detector

with a forward–backward symmetric cylindrical geometry and a near 4π coverage in solid angle [19–21].[1] It consists of an inner tracking detector (ID) surrounded by a thin superconducting solenoid providing a 2 T axial magnetic field, electromagnetic and hadron calorimeters, and a muon spectrometer (MS). The inner tracking detector covers the pseudorapidity range $|\eta| < 2.5$. It consists of silicon pixel, silicon microstrip, and transition radiation tracking detectors. Lead/liquid-argon (LAr) sampling calorimeters provide electromagnetic (EM) energy measurements with high granularity. A steel/scintillator-tile hadron calorimeter covers the central pseudorapidity range ($|\eta| < 1.7$). The endcap and forward regions are instrumented with LAr calorimeters for both the EM and hadronic energy measurements up to $|\eta| = 4.9$. A two-level trigger system is used to select events. The first-level trigger is implemented in hardware and uses a subset of the detector information to accept events at a rate below 100 kHz. This is followed by a software-based trigger that reduces the accepted event rate to 1 kHz on average depending on the data-taking conditions. An extensive software suite [22] is used in the reconstruction and analysis of real and simulated data, in detector operations, and in the trigger and data acquisition systems of the experiment.

The Monte Carlo (MC) simulated signal samples were generated using MadGraph5_aMC@NLO [23], with matrix elements (ME) calculated at the leading order (LO) in perturbative QCD and with the `NNPDF3.0nlo` [24] parton distribution function (PDF) set. The events were interfaced to Pythia 8.230 [25] to model the parton shower, hadronization, and underlying event, with parameters set according to the A14 tuned parton-shower parameter (tune) [26] and using the NNPDF2.3lo [27] set of PDFs. Benchmark signal samples were generated with $\alpha_D = 0.1$ and $\epsilon = 10^{-3}$, in the mass ranges of 5 GeV $< m_{A'} <$ 40 GeV and 20 GeV $< m_{h_D} <$ 70 GeV. The dominant SM background process, $q\bar{q} \to 4\ell$, was simulated with the Sherpa 2.2.2 event generator [28]. Matrix elements were calculated at next-to-leading-order (NLO) accuracy in QCD for up to one additional parton and at LO accuracy for two and three additional parton emissions. The matrix element calculations were matched and merged with the Sherpa parton shower based on Catani–Seymoour dipole factorization [29, 30], using the MEPS@NLO prescription [31–34]. An alternative $q\bar{q} \to 4\ell$ sample for estimating the theory modeling uncertainty was generated at NLO accuracy in QCD using Powheg Box v2 [35–37], interfaced to Pythia 8.186 [38] for the modeling of the parton shower, hadronization, and underlying event, with parameters set according to the AZNLO tune [39]. The `CT10` PDF set [40] was used for the hard-scattering processes, whereas the `CTEQ6L1` PDF set [41] was used for the parton shower. The real higher-order electroweak contribution to 4ℓ production in association with two jets (which includes vector-boson scattering, but excludes processes involving the Higgs boson) was not included in the sample discussed above but was simulated separately with the Sherpa 2.2.2 generator. Sherpa 2.2.2 was also used for the $gg \to ZZ$ production, with LO precision for zero- and one-jet final states, where a constant k-factor of 1.7 [42] is applied to account for NLO effects on the cross-section. The resonant $H \to ZZ^* \to 4\ell$ process was generated independently to provide the highest possible precision. The dominant gluon-fusion [43] and vector boson fusion (VBF) [44] processes are modeled with Powheg Box v2. The gluon-fusion sample uses Powheg-NNLOPS [45–48] to achieve inclusive NNLO QCD precision. Four or more prompt leptons can also be produced by a number of triboson processes, ZWW, ZZW and ZZZ, and by Z bosons produced in association with a $t\bar{t}$ pair ($t\bar{t}Z$). Samples for these processes were simulated with Sherpa 2.2.2 and Sherpa 2.2.0 for triboson and $t\bar{t}Z$, respectively.

Except for the signal, all samples were produced with a detailed simulation of the ATLAS detector [49]

[1] ATLAS uses a right-handed coordinate system with its origin at the nominal IP in the center of the detector and the z-axis along the beam pipe.The x-axis points from the IP to the center of the LHC ring, and the y-axis points upward. Cylindrical coordinates (r, ϕ) are used in the transverse plane, ϕ being the azimuthal angle around the z-axis. The pseudorapidity is defined in terms of the polar angle θ as $\eta = -\ln\tan\theta/2$. Angular distance is measured in units of $\Delta R \equiv \sqrt{(\Delta\eta)^2 + (\Delta\phi)^2}$.

based on GEANT4 [50], to produce predictions that can be used to compare with the data. The signal samples were produced through a simplified simulation of the ATLAS detector [49]. Furthermore, simulated inelastic minimum-bias events were overlaid to model additional pp collisions in the same and neighbouring bunch crossings (pile-up) [51]. Simulated events were reweighted to match the pile-up conditions in the data. All simulated events were processed using the same reconstruction algorithms as used in data.

Events are required to have a collision vertex associated with at least two tracks, each with a transverse momentum $p_{\mathrm{T}} > 0.5$ GeV. The vertex with the highest sum of squared transverse momentum of the associated tracks is referred to as the primary vertex. Muon candidates within the range $|\eta| < 2.5$ are reconstructed by combining ID and MS information [52]. In the region $2.5 < |\eta| < 2.7$, muons can also be identified by tracks of the muon spectrometer alone. In the region $|\eta| < 0.1$, muons are identified by an ID track with $p_{\mathrm{T}} > 15$ GeV associated with a compatible calorimeter energy deposit. Muons are required to have $p_{\mathrm{T}} > 3$ GeV, $|\eta| < 2.7$ and satisfy the 'loose' identification critt erion [52]. Electrons are reconstructed from energy deposits in the EM calorimeter matched to a track in the ID [53]. Candidate electrons must have $p_{\mathrm{T}} > 4.5$ GeV and $|\eta| < 2.47$, and satisfy the 'loose' identification criteria [53]. All electrons and muons must be isolated and satisfy the 'FixedCutLoose' and 'PflowLoose_VarRad' isolation criteria [53, 54], respectively. Furthermore, electrons (muons) are required to have associated tracks satisfying $|d_0|/\sigma_{d_0} < 5$ (3) and $|z_0 \sin(\theta)| < 0.5$ mm, where d_0 is the transverse impact parameter relative to the beam line, σ_{d_0} is its uncertainty, and z_0 is the longitudinal impact parameter relative to the primary vertex.

Jets are reconstructed with the anti-k_t algorithm [55, 56] with a radius parameter of $R = 0.4$. The jet clustering input objects are based on particle-flow [57] in the ID and the calorimeter. Jets are required to have $p_{\mathrm{T}} > 30$ GeV and $|\eta| < 4.5$. A jet-vertex tagger [58] is applied to jets with $p_{\mathrm{T}} < 60$ GeV and $|\eta| < 2.4$ to preferentially suppress jets that originated from pile-up. An overlap-removal procedure detailed in Ref. [59] is applied to the selected leptons and jets, to avoid ambiguities in the event selection and in the energy measurement of the physics objects.

Candidate events are selected by requiring at least two same-flavor and opposite-charge (SFOC) lepton pairs. The four-lepton invariant mass must satisfy $m_{4\ell} < m_Z - 5$ GeV to suppress the SM $pp \to 4\ell$ background. If more than one lepton quadruplet is selected in an event, the one with the smallest lepton-pair mass difference $|m_{\ell^+\ell^-} - m_{\ell'^+\ell'^-}|$, where $m_{\ell^+\ell^-}$ and $m_{\ell'^+\ell'^-}$ are the invariant masses of the two SFOC lepton pairs in the quadruplet, is selected. To ensure both SFOC lepton pairs from the signal originate from an A' decay and to reduce the mispairing effect, the dilepton masses are required to satisfy $m_{\ell_3\ell_4}/m_{\ell_1\ell_2} > 0.85$. All the same (different) flavored leptons are required to have an angular separation of $\Delta R > 0.1$ (0.2). The two SFOC lepton pairs (and the two pairs with the alternative opposite-charge pairing, in the case of $4e$ and 4μ final states), within a quadruplet are required to have a dilepton mass $m_{\ell^+\ell^-} > 5$ GeV, and events with $(m_{\Upsilon(1S)} - 0.70\ \mathrm{GeV}) < m_{\ell^+\ell^-} < (m_{\Upsilon(3S)} + 0.75\ \mathrm{GeV})$ are vetoed to suppress the quarkonia background.

Events passing the above selections, referred to as the signal region (SR), are used to search for the dark photon. The dominant background contribution in the SR is from the $qq \to 4\ell$ process. The kinematic distributions of the $qq \to 4\ell$ background are modeled using simulation, while the background event yield is normalized to data with the help of a control region (CR) enriched in $qq \to 4\ell$ events. The CR is defined similarly to the SR but with $m_Z - 5$ GeV $< m_{4\ell} < m_Z + 5$ GeV, and the $m_{\ell_3\ell_4}/m_{\ell_1\ell_2}$ and Υ veto requirements are not applied. The modeling of the kinematic properties of the $qq \to 4\ell$ background is studied in a validation region (VR), which is orthogonal to both the SR and the CR. The VR is defined using the same selections as for the SR except for requiring $m_{\ell_3\ell_4}/m_{\ell_1\ell_2} < 0.85$.

Subleading background originates from processes involving the production of Z + jets, top-quark and $WZjj$, with non-prompt leptons from hadron decays or misidentified from jets. A fake factor method as described in Ref. [60] is used to estimate the contributions from non-prompt leptons. The fake factor is defined as the ratio of numbers of non-promptn leptons $N_{\text{fake}}^{\text{tight}}/N_{\text{fake}}^{\text{loose}}$, where 'tight' or 'loose' indicate whether those leptons pass all the requirements on the impact parameters, isolation and identification or not. The fake factor is measured in Z + jets events using additional leptons other than the lepton pair arising from the Z boson decay. The non-prompt lepton background is then estimated by applying the fake factor in a region defined with the same event selection as the SR, but with at least one loose-not-tight lepton required to form the quadruplet. Minor background contributions from $pp \to H \to 4\ell$, the $gg \to ZZ \to 4\ell$ continuum, triboson and ttZ processes are estimated from simulation, and their event yield contribution is found to be about 5% in the SR.

The search sensitivity is limited by statistical uncertainties. Systematic uncertainties associated with the prediction of signal and background processes are also considered. These uncertainties are either experimental or theoretical in nature, due to imperfect modeling of the detector in the simulation or the underlying physics of each process. Experimental uncertainties mainly originate from energy measurements of leptons, and efficiencies of lepton reconstruction and identification. Uncertainties due to the trigger selection efficiency, pile-up correction, and luminosity measurement are also considered. Overall, the total experimental uncertainty in the predicted yields is about 6% for both the signal and backgrounds with prompt leptons. The theoretical uncertainties of the signal, as well as the major background of the $qq \to 4\ell$ process, include the uncertainties from PDFs, QCD scales, and α_S. The PDF uncertainty is estimated following the PDF4LHC [61] procedure. The α_S uncertainty is estimated by varying the α_S value by ± 0.001. The QCD scale uncertainty is estimated by varying the renormalization and factorization scales following the procedure described in Ref. [62]. The parton showering and hadronization uncertainty is estimated for the signal by comparing the nominal Pythia 8 parton showering with the alternative Herwig 7 [63, 64] algorithm. For the $qq \to 4\ell$ background, the modeling uncertainty due to the matrix element, showering, and hadronization is obtained by comparing predictions between the nominal Sherpa sample and an alternative sample generated by Powheg Box v2 interfaced with Pythia 8. Modeling uncertainties in the p_{T}^{Z} distribution for the signal process, which is simulated at the LO, are also considered. The total theoretical uncertainties in the reconstructed event yields for the signal and the $qq \to 4\ell$ background processes are estimated to be about 14% and 13%, respectively. Systematic uncertainties assigned to the fake lepton background mainly account for differences in the composition of the events with fake leptons between Z + jets events and the events in the SR, and data statistical uncertainties in the dedicated region where fake factors are applied. They are estimated to be about 51% and 41%, respectively.

A simultaneous profiled binned maximum-likelihood fit [65–67] to the average invariant mass $\bar{m}_{\ell\ell}$, $\bar{m}_{\ell\ell} = (m_{\ell_1\ell_2} + m_{\ell_3\ell_4})/2$, of events in the SR and CR is performed to constrain uncertainties and extract evidence of a possible signal. The normalizations of both the signal and the $qq \to 4\ell$ background are allowed to float in the fit. Systematic uncertainties described above are modeled as constrained nuisance parameters.

Table 1 shows the estimated and observed event yields in the SR, CR and VR after a background-only fit. The $\bar{m}_{\ell\ell}$ distributions in the SR, CR and VR are presented in Fig. 2. The data are found to be consistent with the background expectation in all three regions. No significant deviation from the SM background hypothesis is observed. Exclusion limits are set using the CL_s prescription [68]. Upper limits at 95% confidence level (CL) on the cross-section times branching fraction of the process $pp \to Z \to A'h_{\text{D}} \to 4\ell + X$ are shown in Fig. 3 for different masses of h_{D}. Based on the assumption that the mixing between the SM and dark Higgs bosons is not considered, and that the dark photon is the lightest particle in the DS, the branching

fractions of the dark Higgs boson decaying into a dark photon pair, as well as of the dark photon decaying into SM fermion pairs are set to 100%. In this dark Abelian Higgs model, upper limits at 90% CL are also set on the combined parameter $\alpha_D \epsilon^2$, which scales the signal yield linearly, as shown in Fig. 4. The search is sensitive to a set of $m_{A'}$ and m_{h_D} masses complementary to, and higher than, a similar search reported by the Belle collaboration [13].

Table 1: Numbers of estimated post-fit background events and observed events in the SR, CR and VR. The 'Fake' background represents the contribution from lepton misidentification, and the 'Others' category combines $gg \to ZZ$, VVV and ttZ background contributions. The expected signal yields for two benchmark points are also shown, with cross-sections calculated with $\alpha_D = 0.1$ and $\epsilon = 10^{-3}$, and they are negligible in the CR and VR.

SM backgrounds	SR	CR	VR
$qq \to 4\ell$	26.0 ± 2.4	1555 ± 48	239 ± 15
Fake	13.2 ± 5.6	43 ± 25	47 ± 26
Others	2.2 ± 0.7	5.8 ± 1.9	6.8 ± 2.0
Total background	41.3 ± 5.3	1604 ± 40	293 ± 28
Data	44	1602	286
Signal ($m_{A'}$, m_{h_D}) = (12, 30) GeV	5.9 ± 0.9	-	-
Signal ($m_{A'}$, m_{h_D}) = (25, 60) GeV	3.5 ± 0.6	-	-

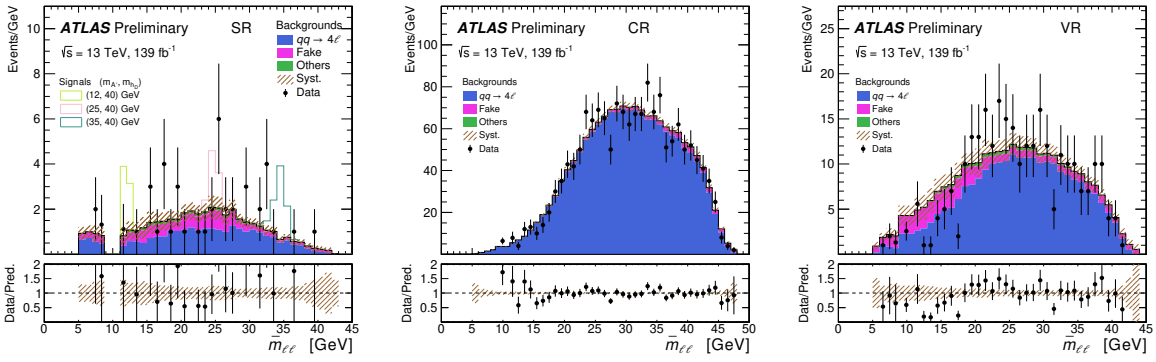

(a) (b) (c)

Figure 2: The $\bar{m}_{\ell\ell}$ distribution in the (a) SR, (b) CR and (c) VR for the data and post-fit background contributions. The error bands include experimental and theoretical systematic uncertainties as constrained after a background-only fit. The contributions from the production of $qq \to 4\ell$ events are scaled by a normalization factor 0.95, from the simultaneous fit in the SR and CR. The 'Others' category combines $gg \to ZZ$, VVV and ttZ background contributions. The 'Fake' background represents the contribution from lepton mis-identification. Representative signal distributions are overlaid in the SR, with the assumption of $m_{h_D} = 40$ GeV and different values of $m_{A'}$. The cross-sections for these benchmark points are calculated with $\alpha_D = 0.1$ and $\epsilon = 10^{-3}$.

In conclusion, this note reports the first search for a dark photon and dark Higgs boson produced via the dark Higgs-strahlung process in rare Z boson decays at the LHC, with a final state of at least four charged leptons and using 139 fb^{-1} of $\sqrt{s} = 13$ TeV pp collision data recorded by the ATLAS detector. The data are found to be consistent with the background prediction. Upper limits are set on the production cross-section times branching fraction, $\sigma(pp \to Z \to A' h_D \to 4\ell + X)$, and dark photon coupling to the dark Higgs boson times the kinetic mixing between the Standard Model photon and the dark photon, $\alpha_D \epsilon^2$, in the mass ranges of 5 GeV $< m_{A'} <$ 40 GeV and 20 GeV $< m_{h_D} <$ 70 GeV. These limits cover significantly

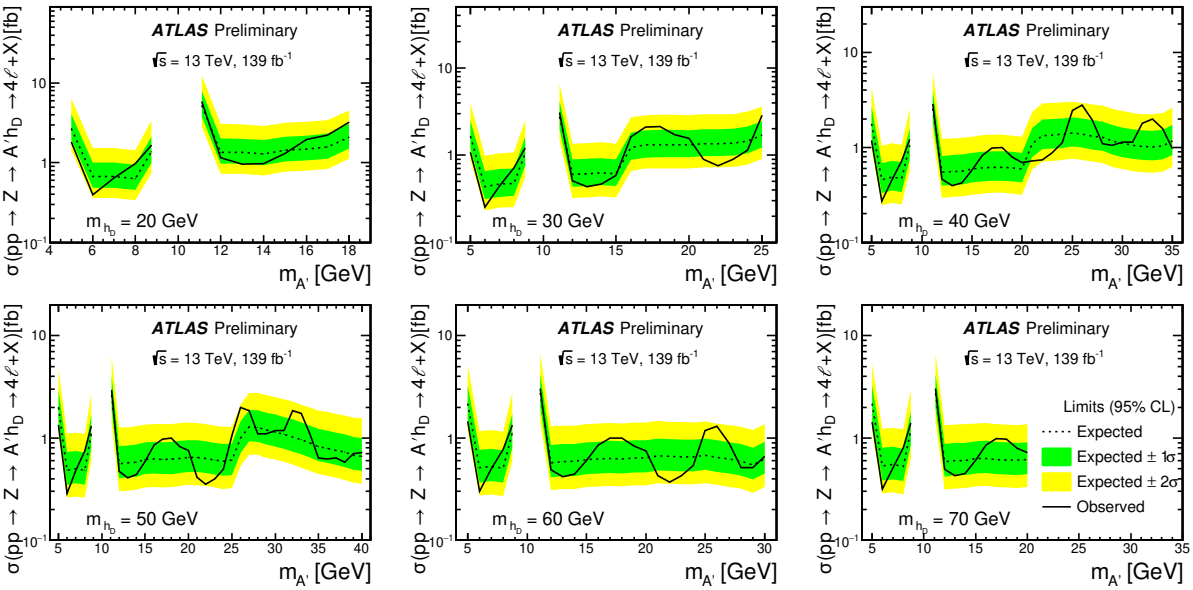

Figure 3: Observed and expected upper limits at 95% CL on the production cross-section times branching fraction as a function of $m_{A'}$, from top left to bottom right, corresponding to the dark Higgs boson mass of 20 GeV, 30 GeV, 40 GeV, 50 GeV, 60 GeV, and 70 GeV, respectively. The green (inner) and yellow (outer) bands represent the $\pm 1\sigma$ and $\pm 2\sigma$ uncertainty in the expected limits.

wider mass ranges than previous experiments.

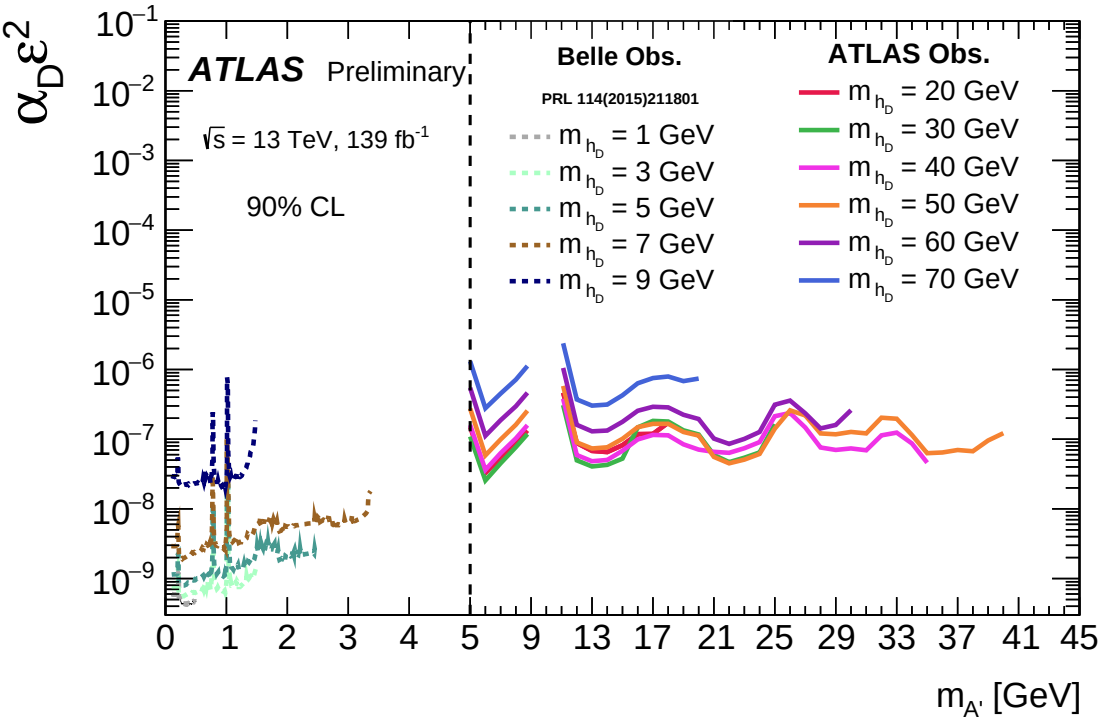

Figure 4: Observed 90% CL upper limits on $\alpha_D \epsilon^2$, as a function of $m_{A'}$ with different dark Higgs boson masses, from this search (solid curves) compared to the results from Belle [13] (dashed curves).

Acknowledgements

References

[1] J. Silk et al., *Particle Dark Matter: Observations, Models and Searches*, ed. by G. Bertone, Cambridge: Cambridge Univ. Press, 2010, ISBN: 978-1-107-65392-4 (cit. on p. 2).

[2] J. L. Feng, *Dark Matter Candidates from Particle Physics and Methods of Detection*, Ann. Rev. Astron. Astrophys. **48** (2010) 495, arXiv: 1003.0904 [astro-ph.CO] (cit. on p. 2).

[3] T. A. Porter, R. P. Johnson and P. W. Graham, *Dark Matter Searches with Astroparticle Data*, Ann. Rev. Astron. Astrophys. **49** (2011) 155, arXiv: 1104.2836 [astro-ph.HE] (cit. on p. 2).

[4] G. Bertone et al., *Identifying WIMP dark matter from particle and astroparticle data*, JCAP **03** (2018) 026, arXiv: 1712.04793 [hep-ph] (cit. on p. 2).

[5] B. Batell, M. Pospelov and A. Ritz, *Probing a Secluded U(1) at B-factories*, Phys. Rev. D **79** (2009) 115008, arXiv: 0903.0363 [hep-ph] (cit. on p. 2).

[6] N. Blinov, E. Izaguirre and B. Shuve, *Rare Z Boson Decays to a Hidden Sector*, Phys. Rev. D **97** (2018) 015009, arXiv: 1710.07635 [hep-ph] (cit. on p. 2).

[7] L. Marsicano et al., *Dark photon production through positron annihilation in beam-dump experiments*, Phys. Rev. D **98** (2018) 015031, arXiv: 1802.03794 [hep-ex] (cit. on p. 2).

[8] J. D. Bjorken, R. Essig, P. Schuster and N. Toro, *New Fixed-Target Experiments to Search for Dark Gauge Forces*, Phys. Rev. D **80** (2009) 075018, arXiv: 0906.0580 [hep-ph] (cit. on p. 2).

[9] A. Anastasi et al., *Limit on the production of a new vector boson in* $e^+e^- \to U\gamma$, $U \to \pi^+\pi^-$ *with the KLOE experiment*, Phys. Lett. B **757** (2016) 356, arXiv: 1603.06086 [hep-ex] (cit. on p. 2).

[10] LHCb Collaboration, *Search for* $A' \to \mu^+\mu^-$ *Decays*, Phys. Rev. Lett. **124** (2020) 041801, arXiv: 1910.06926 [hep-ex] (cit. on p. 2).

[11] CMS Collaboration, *Search for a Narrow Resonance Lighter than* 200 *GeV Decaying to a Pair of Muons in Proton–Proton Collisions at* $\sqrt{s} = 13$ *TeV*, Phys. Rev. Lett. **124** (2020) 131802, arXiv: 1912.04776 [hep-ex] (cit. on p. 2).

[12] J. P. Lees et al., *Search for Low-Mass Dark-Sector Higgs Bosons*, Phys. Rev. Lett. **108** (2012) 211801, arXiv: 1202.1313 [hep-ex] (cit. on p. 2).

[13] I. Jaegle, *Search for the dark photon and the dark Higgs boson at Belle*, Phys. Rev. Lett. **114** (2015) 211801, arXiv: 1502.00084 [hep-ex] (cit. on pp. 2, 6, 8).

[14] D. Curtin, R. Essig, S. Gori and J. Shelton, *Illuminating Dark Photons with High-Energy Colliders*, JHEP **02** (2015) 157, arXiv: 1412.0018 [hep-ph] (cit. on p. 2).

[15] *Luminosity determination in* pp *collisions at* $\sqrt{s} = 13$ *TeV using the ATLAS detector at the LHC*, (2022), arXiv: 2212.09379 [hep-ex] (cit. on p. 2).

[16] ATLAS Collaboration, *ATLAS data quality operations and performance for 2015–2018 data-taking*, JINST **15** (2020) P04003, arXiv: 1911.04632 [physics.ins-det] (cit. on p. 2).

[17] ATLAS Collaboration, *Performance of the ATLAS muon triggers in Run 2*, JINST **15** (2020) P09015, arXiv: 2004.13447 [hep-ex] (cit. on p. 2).

[18] ATLAS Collaboration, *Performance of electron and photon triggers in ATLAS during LHC Run 2*, Eur. Phys. J. C **80** (2020) 47, arXiv: 1909.00761 [hep-ex] (cit. on p. 2).

[19] ATLAS Collaboration, *The ATLAS Experiment at the CERN Large Hadron Collider*, JINST **3** (2008) S08003 (cit. on p. 3).

[20] ATLAS Collaboration, *ATLAS Insertable B-Layer Technical Design Report*, ATLAS-TDR-19; CERN-LHCC-2010-013, 2010, URL: https://cds.cern.ch/record/1291633 (cit. on p. 3), Addendum: ATLAS-TDR-19-ADD-1; CERN-LHCC-2012-009, 2012, URL: https://cds.cern.ch/record/1451888.

[21] B. Abbott et al., *Production and integration of the ATLAS Insertable B-Layer*, JINST **13** (2018) T05008, arXiv: 1803.00844 [physics.ins-det] (cit. on p. 3).

[22] ATLAS Collaboration, *The ATLAS Collaboration Software and Firmware*, ATL-SOFT-PUB-2021-001, 2021, URL: https://cds.cern.ch/record/2767187 (cit. on p. 3).

[23] J. Alwall et al., *The automated computation of tree-level and next-to-leading order differential cross sections, and their matching to parton shower simulations*, JHEP **07** (2014) 079, arXiv: 1405.0301 [hep-ph] (cit. on p. 3).

[24] R. D. Ball et al., *Parton distributions for the LHC run II*, JHEP **04** (2015) 040, arXiv: 1410.8849 [hep-ph] (cit. on p. 3).

[25] T. Sjöstrand et al., *An introduction to PYTHIA 8.2*, Comput. Phys. Commun. **191** (2015) 159, arXiv: 1410.3012 [hep-ph] (cit. on p. 3).

[26] ATLAS Collaboration, *ATLAS Pythia 8 tunes to 7 TeV data*, ATL-PHYS-PUB-2014-021, 2014, URL: https://cds.cern.ch/record/1966419 (cit. on p. 3).

[27] R. D. Ball et al., *Parton distributions with LHC data*, Nucl. Phys. B **867** (2013) 244, arXiv: 1207.1303 [hep-ph] (cit. on p. 3).

[28] E. Bothmann et al., *Event generation with Sherpa 2.2*, SciPost Phys. **7** (2019) 034, arXiv: 1905.09127 [hep-ph] (cit. on p. 3).

[29] T. Gleisberg and S. Höche, *Comix, a new matrix element generator*, JHEP **12** (2008) 039, arXiv: 0808.3674 [hep-ph] (cit. on p. 3).

[30] S. Schumann and F. Krauss, *A parton shower algorithm based on Catani–Seymour dipole factorisation*, JHEP **03** (2008) 038, arXiv: 0709.1027 [hep-ph] (cit. on p. 3).

[31] S. Höche, F. Krauss, M. Schönherr and F. Siegert, *A critical appraisal of NLO+PS matching methods*, JHEP **09** (2012) 049, arXiv: 1111.1220 [hep-ph] (cit. on p. 3).

[32] S. Höche, F. Krauss, M. Schönherr and F. Siegert, *QCD matrix elements + parton showers. The NLO case*, JHEP **04** (2013) 027, arXiv: 1207.5030 [hep-ph] (cit. on p. 3).

[33] S. Catani, F. Krauss, B. R. Webber and R. Kuhn, *QCD Matrix Elements + Parton Showers*, JHEP **11** (2001) 063, arXiv: hep-ph/0109231 (cit. on p. 3).

[34] S. Höche, F. Krauss, S. Schumann and F. Siegert, *QCD matrix elements and truncated showers*, JHEP **05** (2009) 053, arXiv: 0903.1219 [hep-ph] (cit. on p. 3).

[35] S. Alioli, P. Nason, C. Oleari and E. Re, *A general framework for implementing NLO calculations in shower Monte Carlo programs: the POWHEG BOX*, JHEP **06** (2010) 043, arXiv: 1002.2581 [hep-ph] (cit. on p. 3).

[36] T. Melia, P. Nason, R. Rontsch and G. Zanderighi, *W^+W^-, WZ and ZZ production in the POWHEG BOX*, JHEP **11** (2011) 078, arXiv: 1107.5051 [hep-ph] (cit. on p. 3).

[37] P. Nason and G. Zanderighi, *W^+W^-, WZ and ZZ production in the POWHEG-BOX-V2*, Eur. Phys. J. C **74** (2014) 2702, arXiv: 1311.1365 [hep-ph] (cit. on p. 3).

[38] T. Sjöstrand, S. Mrenna and P. Skands, *A brief introduction to PYTHIA 8.1*, Comput. Phys. Commun. **178** (2008) 852, arXiv: 0710.3820 [hep-ph] (cit. on p. 3).

[39] ATLAS Collaboration, *Measurement of the Z/γ^* boson transverse momentum distribution in pp collisions at $\sqrt{s} = 7$ TeV with the ATLAS detector*, JHEP **09** (2014) 145, arXiv: 1406.3660 [hep-ex] (cit. on p. 3).

[40] H.-L. Lai et al., *New parton distributions for collider physics*, Phys. Rev. D **82** (2010) 074024, arXiv: 1007.2241 [hep-ph] (cit. on p. 3).

[41] J. Pumplin et al., *New Generation of Parton Distributions with Uncertainties from Global QCD Analysis*, JHEP **07** (2002) 012, arXiv: hep-ph/0201195 (cit. on p. 3).

[42] F. Caola, K. Melnikov, R. Röntsch and L. Tancredi, *QCD corrections to ZZ production in gluon fusion at the LHC*, Phys. Rev. D **92** (2015) 094028, arXiv: 1509.06734 [hep-ph] (cit. on p. 3).

[43] K. Hamilton, P. Nason, E. Re and G. Zanderighi, *NNLOPS simulation of Higgs boson production*, JHEP **10** (2013) 222, arXiv: 1309.0017 [hep-ph] (cit. on p. 3).

[44] P. Nason and C. Oleari, *NLO Higgs boson production via vector-boson fusion matched with shower in POWHEG*, JHEP **02** (2010) 037, arXiv: 0911.5299 [hep-ph] (cit. on p. 3).

[45] K. Hamilton, P. Nason, E. Re and G. Zanderighi, *NNLOPS simulation of Higgs boson production*, JHEP **10** (2013) 222, arXiv: 1309.0017 [hep-ph] (cit. on p. 3).

[46] K. Hamilton, P. Nason and G. Zanderighi, *Finite quark-mass effects in the NNLOPS POWHEG+MiNLO Higgs generator*, JHEP **05** (2015) 140, arXiv: 1501.04637 [hep-ph] (cit. on p. 3).

[47] D. de Florian et al., *Handbook of LHC Higgs Cross Sections: 4. Deciphering the Nature of the Higgs Sector*, (2016), arXiv: 1610.07922 [hep-ph] (cit. on p. 3).

[48] C. Anastasiou et al., *High precision determination of the gluon fusion Higgs boson cross-section at the LHC*, JHEP **05** (2016) 058, arXiv: 1602.00695 [hep-ph] (cit. on p. 3).

[49] ATLAS Collaboration, *The ATLAS Simulation Infrastructure*, Eur. Phys. J. C **70** (2010) 823, arXiv: 1005.4568 [physics.ins-det] (cit. on pp. 3, 4).

[50] GEANT4 Collaboration, S. Agostinelli et al., *GEANT4 – a simulation toolkit*, Nucl. Instrum. Meth. A **506** (2003) 250 (cit. on p. 4).

[51] ATLAS Collaboration, *Emulating the impact of additional proton–proton interactions in the ATLAS simulation by pre-sampling sets of inelastic Monte Carlo events*, Comput. Softw. Big Sci. **6** (2021) 3, arXiv: 2102.09495 [hep-ex] (cit. on p. 4).

[52] ATLAS Collaboration, *Muon reconstruction performance of the ATLAS detector in proton–proton collision data at* $\sqrt{s} = 13$ *TeV*, Eur. Phys. J. C **76** (2016) 292, arXiv: 1603.05598 [hep-ex] (cit. on p. 4).

[53] ATLAS Collaboration, *Electron and photon performance measurements with the ATLAS detector using the 2015–2017 LHC proton–proton collision data*, JINST **14** (2019) P12006, arXiv: 1908.00005 [hep-ex] (cit. on p. 4).

[54] ATLAS Collaboration, *Muon reconstruction and identification efficiency in ATLAS using the full Run 2 pp collision data set at* $\sqrt{s} = 13$ *TeV*, Eur. Phys. J. C **81** (2021) 578, arXiv: 2012.00578 [hep-ex] (cit. on p. 4).

[55] ATLAS Collaboration, *Track assisted techniques for jet substructure*, ATL-PHYS-PUB-2018-012, 2018, URL: https://cds.cern.ch/record/2630864 (cit. on p. 4).

[56] M. Cacciari, G. P. Salam and G. Soyez, *FastJet user manual*, Eur. Phys. J. C **72** (2012) 1896, arXiv: 1111.6097 [hep-ph] (cit. on p. 4).

[57] ATLAS Collaboration, *Jet reconstruction and performance using particle flow with the ATLAS Detector*, Eur. Phys. J. C **77** (2017) 466, arXiv: 1703.10485 [hep-ex] (cit. on p. 4).

[58] ATLAS Collaboration, *Performance of pile-up mitigation techniques for jets in pp collisions at* $\sqrt{s} = 8$ *TeV using the ATLAS detector*, Eur. Phys. J. C **76** (2016) 581, arXiv: 1510.03823 [hep-ex] (cit. on p. 4).

[59] ATLAS Collaboration, *Higgs boson production cross-section measurements and their EFT interpretation in the* 4ℓ *decay channel at* $\sqrt{s} = 13$ *TeV with the ATLAS detector*, Eur. Phys. J. C **80** (2020) 957, arXiv: 2004.03447 [hep-ex] (cit. on p. 4), Erratum: Eur. Phys. J. C **81** (2021) 29.

[60] ATLAS Collaboration, $ZZ \to \ell^+\ell^-\ell'^+\ell'^-$ *cross-section measurements and search for anomalous triple gauge couplings in* 13 *TeV pp collisions with the ATLAS detector*, Phys. Rev. D **97** (2018) 032005, arXiv: 1709.07703 [hep-ex] (cit. on p. 5).

[61] J. Butterworth et al., *PDF4LHC recommendations for LHC Run II*, J. Phys. G **43** (2016) 023001, arXiv: 1510.03865 [hep-ph] (cit. on p. 5).

[62] ATLAS Collaboration, *Measurement of ZZ production in the* $\ell\ell\nu\nu$ *final state with the ATLAS detector in pp collisions at* $\sqrt{s} = 13$ *TeV*, JHEP **10** (2019) 127, arXiv: 1905.07163 [hep-ex] (cit. on p. 5).

[63] J. Bellm et al., *Herwig 7.0/Herwig++ 3.0 release note*, Eur. Phys. J. C **76** (2016) 196, arXiv: 1512.01178 [hep-ph] (cit. on p. 5).

[64] M. Bähr et al., *Herwig++ physics and manual*, Eur. Phys. J. C **58** (2008) 639, arXiv: 0803.0883 [hep-ph] (cit. on p. 5).

[65] L. Moneta et al., *The RooStats Project*, PoS **ACAT2010** (2010) 057, arXiv: 1009.1003 [physics.data-an] (cit. on p. 5).

[66] W. Verkerke and D. P. Kirkby, *The RooFit toolkit for data modeling*, eConf **C0303241** (2003) MOLT007, arXiv: physics/0306116 (cit. on p. 5).

[67] K. Cranmer, G. Lewis, L. Moneta, A. Shibata and W. Verkerke, *HistFactory: A tool for creating statistical models for use with RooFit and RooStats*, tech. rep., New York U., 2012, URL: https://cds.cern.ch/record/1456844 (cit. on p. 5).

[68] A. L. Read, *Presentation of search results: the CL_S technique*, J. Phys. G **28** (2002) 2693 (cit. on p. 5).

Appendix

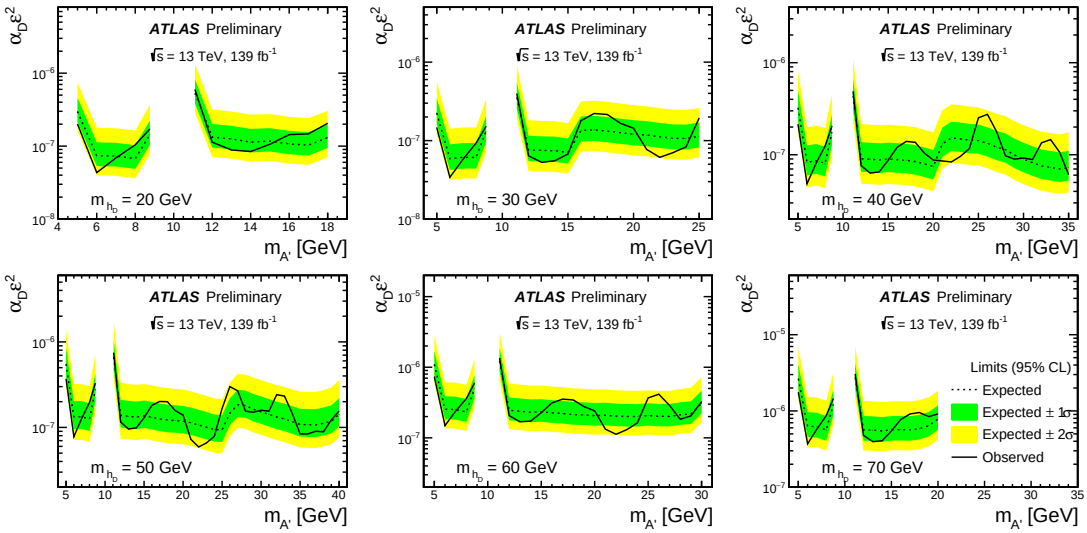

Figure 5: Observed (black solid curve) and expected upper limits (black dashed curve) at 95% CL on $\alpha_D\epsilon^2$ as a function of $m_{A'}$, from top left to bottom right, corresponding to the dark Higgs boson mass of 20 GeV, 30 GeV, 40 GeV, 50 GeV, 60 GeV and 70 GeV, respectively. The green (inner) and yellow (outer) bands represent $\pm 1\sigma$ and $\pm 2\sigma$ uncertainty in the expected limits.

Table 2: The relative efficiencies of each event selection for the simulated dark photon signal samples, which were generated with $m_{h_D} = 50$ GeV. The efficiencies of an event filter, which was applied at the event generator level, requiring at least four leptons with $p_T > 2$ GeV and $|\eta| < 3.0$, are listed in the table as well. The overall signal efficiencies are the products of the event filter efficiency and the efficiency of each event selection.

$m_{A'}$ [GeV]	8	15	20	30	40
MC filter efficiency	58.0%	62.2%	64.5%	60.6%	53.2%
Number of identified leptons ≥ 4	27.2%	26.9%	28.4%	15.1%	15.7%
$m_{4\ell} < m_Z - 5$ GeV	96.9%	98.0%	98.8%	98.3%	85.4%
Number of SFOC lepton pairs ≥ 2	73.1%	74.4%	77.6%	82.2%	85.7%
$m_{\ell_3\ell_4}/m_{\ell_1\ell_2} > 0.85$	86.2%	86.7%	87.4%	80.4%	87.0%
$m_{\ell^+\ell^-}$ outside [0, 5] and [8.76, 11.105] GeV	92.0%	91.7%	90.1%	93.7%	95.8%
Trigger	70.0%	63.3%	59.2%	69.5%	82.0%
Combined event selection efficiency	10.7%	9.9%	10.1%	6.4%	7.9%
Overall dark photon signal efficiency	6.2%	6.2%	6.5%	3.9%	4.2%